Chem Soc Rev

Chemical Dynamics Simulations of Energy Transfer, Fragmentation, and Reaction in Collisions of Protonated Peptide Ions with Organic Surfaces

Journal:	*Chemical Society Reviews*
Manuscript ID	CS-TRV-06-2015-000482.R2
Article Type:	Tutorial Review
Date Submitted by the Author:	30-Oct-2015
Complete List of Authors:	Pratihar, Subha; Texas Tech. University, Chemistry and Biochemistry Barnes, George; Siena College, Chemistry and Biochemistry Hase, William; Texas Tech University, Dept of Chemistry and Biochemistry

Chemical Dynamics Simulations of Energy Transfer, Surface-Induced Dissociation, Soft-Landing, and Reactive-Landing in Collisions of Protonated Peptide Ions with Organic Surfaces

Subha Pratihar[a], George L. Barnes[b] and William L. Hase[a,*]

[a]Department of Chemistry and Biochemistry
Texas Tech University
Lubbock, TX 79409–1061, USA

[b]Department of Chemistry and Biochemistry
Siena College
Loudonville, NY 12211, USA

* To whom correspondence should be addressed: bill.hase@ttu.edu

Abstract

There are two components to the review presented here regarding simulations of collisions of protonated peptide ions peptide–H^+ with organic surfaces. One is a detailed description of the classical trajectory chemical dynamics simulation methodology. Different simulation approaches are used, and identified as MM, QM+MM, and QM/MM dependent on the potential energy surface used to represent the peptide–H^+ + surface collision. The second are representative examples of the information that may be obtained from the simulations regarding energy transfer and peptide–H^+ surface-induced dissociation, soft-landing, and reactive-landing for the peptide–H^+ + surface collisions. Good agreement with experiment is obtained for each of these four collision properties. The simulations provide atomistic interpretations of the peptide–H^+ + surface collision dynamics.

I. Introduction

There is a wide interest in understanding the physical and chemical changes that result from collisions between protonated peptide ions (peptide–H^+) and various surfaces. In particular, we will highlight what has been learned regarding collisions with self–assembled monolayers (SAMs), which are important organic surfaces widely used in nanoscience and nanotechnology,[1] and diamond surfaces that have a wide variety of commercial applications in areas such as optical coatings and high temperature electronics.[2]

For the last two decades, peptide/protein collisions with SAM surfaces has been a principal research interest of mass–spectrometry. Several chemical and physical processes may occur when a protonated peptide ion collides with an organic surface. They include surface–induced dissociation (SID),[3,4] reactive–landing (RL),[5] and soft–landing (SL).[6,7] In SID the projectile become sufficiently energized via a collision with the surface, for a collision energy in the 10-150 eV range,[3,4] that it dissociates. SID is an important experimental tool for determining structural properties of ions,[4] as well as providing energetic and mechanistic information concerning their dissociation pathways.[8] SID provides a fingerprint of the ion's structure, and has been studied actively over the past two decades by tandem mass spectrometry.[3] In RL the projectile forms chemical bonds with and chemisorbs on the surface.[9] SL, a process first introduced by Cooks and co–workers in 1977 and characterized for organic ions in 1997,[10] is deposition of intact projectile ions on the surface, with or without charge retention. RL and SL have a number of important applications, including preparation of protein microarrays, development of biosensors and deposition of mass selected cluster ions.[5-7,9,10] Covalent linking of molecules to substrates using RL is a promising method for highly selective surface modification using hyperthermal beams of mass–selected ions.[5,9]

Chemical dynamics simulations have proven to be an important procedure for modeling and interpreting the above experiments.[11-14] They are particularly powerful in providing an atomistic understanding of the peptide–H^+ + surface collision dynamics. The simulations are able to determine energy transfer and fragmentation dynamics for SID, as well as mechanisms for SL and RL. In this review, we describe the methodology of the chemical dynamics simulations, and illustrate some of the important findings from the simulations as well as provide comparisons with experiments.

II. Models for Potential Energy Surfaces

The global potential energy for peptide–H^+ ions colliding with organic surfaces is written as

$$V_{total} = V_{peptide} + V_{surface} + V_{surface,\ peptide} \quad (1)$$

$V_{surface}$ and $V_{peptide}$ are potentials for the surface and peptide–H^+, respectively, and $V_{surface,\ peptide}$ is the interaction between the surface and peptide ion.

V_{total} has been represented using three different models: 1) pure molecular mechanics (MM), 2) mixed quantum mechanical (QM) + MM, and 3) mixed QM/MM. In the pure MM treatment, the potential is represented by analytic functions, making this the most computationally efficient approach. While in theory representing fragmentation of peptide-H^+ and reaction of peptide-H^+ with the surface by analytic functions is possible, in practice it becomes challenging. To overcome this short coming, the QM+MM approach is utilized, in which the intramolecular potential of the peptide, $V_{peptide}$, is treated using a QM approach while the surface, and the interaction between the surface and the peptide, $V_{surface,\ peptide}$, are both treated

at an MM level, i.e. the QM and MM potentials are separable. This treatment allows for the study of SID and SL, but not RL. The QM/MM approach treats the peptide and a portion of the surface at the QM level, which allows for reactivity between the surface and the peptide. The portion of the surface treated at the QM level is termed the 'QM region,' while the remainder of $V_{surface}$ is treated at an MM level. At the boundary between the QM and MM region of the surface, a bond is "cleaved" such that one bonding partner is QM while the other MM, which necessitates the need for a chemical bonding interface between the QM and MM regions. Within this model, $V_{surface,\ peptide}$ has both MM and QM components. The interaction between the peptide and the QM region of the surface is automatically included in the QM calculation, while the interaction between the peptide and the MM region of the surface is identical to that of the QM+MM model. The QM+MM model is more computationally efficient than QM/MM. In the following details of the $V_{peptide}$, $V_{surface}$, and $V_{surface,\ peptide}$ models are described.

A. $V_{surface}$

1. Diamond surface

The same type of model was used for all of the peptide–H^+ + diamond {111} simulations,[11,12,15-18] but the size of the model was changed dependent on the size of the peptide ion. The model used for the diamond {111} surface is hydrogen terminated, with a potential consisting of HC and CC harmonic stretches and HCC and CCC bends, and is written as

$$V_{Diamond} = \sum_{CH} \frac{k_r}{2}(r - r_e)^2 + \sum_{CC} \frac{k_R}{2}(R - R_e)^2 + \sum_{HCC} \frac{k_\varphi}{2}(\varphi - \varphi_e)^2 + \sum_{CCC} \frac{k_\theta}{2}(\theta - \theta_e)^2 \quad (2)$$

The equilibrium coordinates are r_e = 1.08 Å, R_e =1.54 Å, and $\phi_e = \theta_e$ = 109.47°. The force constants were chosen to fit the diamond phonon spectrum[19] and are k_r = 5.01 mdyn Å^{-1}, k_R = 3.18 mdyn Å^{-1}, k_ϕ = 0.725 mdyn–Å rad^{-2} and k_θ = 0.868 mdyn–Å rad^{-2}.

Side and top views of the diamond surface model, used for gly_n–H^+ (n = 1-3 and 5) and ala_2–H^+ collisions,[11,12,15-17] are shown in Figure 1a. The model has eight C–atom layers and consists of 1988 atoms, with a tetrahedral, sp^3 arrangement. The surface is 8 Å in depth and has an area of 32 x 34 Å^2. For simulations of gly_8–H^+, the model was increased to include 12 C–atom layers and 6950 atoms.[18] It is ~ 13 Å in depth and has an area of 51 x 52 Å^2. Massive atoms are connected to the bottom atoms of the surface models, by stiff harmonic potentials, to assure that the surface does not move upon peptide–H^+ collision.

2. SAM surfaces

Self–assembled monolayers consisting of n–hexyl $CH_3(CH_2)_5S$ and n–octyl $CH_3(CH_2)_7S$ thiolates, H–SAMs,[11,20] and perfluorinated n–octyl $CF_3(CF_2)_7S$ thiolate, F–SAM,[13,14,21] adsorbed on a Au{111} surface, have been used to study peptide–H^+ + SAM collisions. Both the H–SAM/Au and F–SAM/Au potentials are analytic and written as a sum of bonded and nonbonded terms; i.e.

$$V_{SAM} = V_{bonded} + V_{nonbonded} \quad (3)$$

V_{bonded} includes all stretch, bend, dihedral, and torsional motions and is written as

$$V_{bonded} = \sum_{Stretches} \frac{k_r}{2}(r - r_e)^2 + \sum_{Bends} \frac{k_\theta}{2}(\theta - \theta_e)^2 + \sum_{Dihedrals} \frac{V_n}{2}[1 - cos(n\varphi - \gamma)] + \sum_{Torsions} \frac{V_r}{2}[1 - cos(3\tau)] \quad (4)$$

where r is the distance between atom pairs, θ a bend angle, ϕ a dihedral angle, and τ the torsional angle for terminal methyl groups. V_{bonded} for the H–SAM is the potential developed by Mar and Klein[22] and Hautman and Klein,[23] with the constraints of the C–H and C–C stretches and C–H bends removed. The parameters for the H–SAM V_{bonded} are discussed in ref. 11. The parameters for the F–SAM V_{bonded} were developed by Borodin et al.[24]

$V_{nonbonded}$ is written as the sum of three different types of interactions, namely atom pairs between nearest neighbor chains (interchain terms), atom pairs within the same chain (intrachain terms), and lastly gold-alkyl terms. The first two types of terms are a sum of a r^{-6} long–range attraction and a short–range Buckingham repulsion; i.e.

$$V(r) = A\exp(-Br) - \frac{C}{r^6} \tag{5}$$

where r is the distance between atom pairs. The A, B, and C non-bonded parameters for the H-SAM are discussed in ref. 11 and those for the F-SAM are given by Borodin et al.[24] The third type of term is a sum of interactions between the $CH_2(CF_2)$ and $CH_3(CF_3)$ groups and the Au surface, and each interaction is given by

$$V(z) = \left[\frac{C_{12}}{(z-z_0)^{12}} + \frac{C_3}{(z-z_0)^3}\right] \tag{6}$$

where z is the shortest distance between one of the atoms of the group and the Au surface. The parameters for this potential were derived by Hautman and Klein.[23]

The complete nonbonded interaction is given by

$$V_{nonbonded} = \sum'_{pairs} V(r) + \sum_{C,H(F)} V(z)$$

(7)

where the first restricted summation takes into account all nearest neighbor interchain pairs and intrachain pairs between atoms separated by three or more C-C bonds of the CH_3-$(CH_2)_n$-S- or CF_3-$(CF_2)_n$-S- chain. For the simulations with the n–octyl thiolate H–SAM,[20] Eq. (6) is replaced by Au–C and Au–H Lennard–Jones terms ($A/r^{12} - B/r^6$); where the respective A (kcal–$Å^{12}$/mole) and B (kcal–$Å^6$/mole) are 106.2338 x 10^4 and 521.0 for Au–C and 121.746 x 10^3 and 141.8 for Au–H.

The S–atoms are adsorbed on an Au{111} single layer, in a rhombic pattern, to correspond to either the H–SAM or F–SAM experimental structure,[25,26] and each S atom interacts with the closest three Au atoms via three individual harmonic stretch potentials chosen to fit *ab initio* calculations.[27] For the H–SAM each S–atom is bonded to the three gold atoms at a 3–fold hollow site on the gold surface. The treatment of the gold layer has been shown to be unimportant[28] for the simulations and it is held rigid. The above potential models give accurate 300 K structures of the H–SAM/Au{111} and F–SAM/Au{111} surfaces,[11,13,14,20,21] in comparison with experiment.[25,26]

Simulations have used two different periodic cell geometries for the H–SAM and both represent an Au {111} surface. The first consists of 43 $CH_3(CH_2)_5S$ chains absorbed on the rigid Au{111} layer,[11] while the second consists of 81 (9x9) $CH_3(CH_2)_5S$ chains absorbed on the rigid Au{111} layer forming a rhombic shape[20] (see Figure 1b). Two-dimensional periodic boundary conditions (PBC) are applied to both cell geometries, and results are insensitive to choice. For

the perfluorinated n–octylthiolate simulations, 108 $CF_3(CF_2)_7S$ chains with a total of 2808 atoms were adsorbed on a rigid Au{111} layer of 441 atoms. Simulations for these models were performed with a two–dimensional PBC applied to the SAM surface. For some of the perfluorinated n–octylthiolate simulations, a rigid border model was also considered for the $CF_3(CF_2)_7$ chains of the F–SAM.[14,21] This model had 46 rigid exterior chains to constrain the motions of the 75 interior free chains, for a total of 121 chains. This rigid border model, and a much smaller one with only a total of 57 chains, gave the same peptide–H^+ + F–SAM collision dynamics as found using the PBC condition.[21]

B. $\boldsymbol{V_{peptide}}$

Two different model types were used for the peptide–H^+ intramolecular potential $V_{peptide}$. One is a molecular mechanical (MM) potential, with parameters given by the AMBER valence force field.[29] The second are quantum mechanical (QM) models[12,13,15-17,20] utilizing AM1, PM3, and RM1 semi–empirical and MP2 electronic structure theories. These QM models are used in QM+MM and QM/MM simulations described below. The AMBER MM analytic potential is given by

$$V_{peptide} = \sum_{Stretches} \frac{k_r}{2}(r - r_e)^2 + \sum_{Bends} \frac{k_\theta}{2}(\theta - \theta_e)^2 + \sum_{Dihedrals} \frac{V_n}{2}[1 - cos(n\varphi - \gamma)] + \sum_{i>j} \left[\frac{A_{ij}}{r_{ij}^{12}} - \frac{B_{ij}}{r_{ij}^{6}} + \frac{q_i q_j}{r_{ij}}\right] \quad (8)$$

This function is quite similar to Eq. (4) above except the last term in Eq. (8), which is the non–bonded interaction, has a Lennard–Jones repulsive potential instead of the Buckingham in Eq. (6) and also contains a 1/r electrostatic term. Non–bonded terms are calculated for all atom pairs that are separated by more than three bonds or are not bonded. The effective charges (q_i, q_j), for

the AMBER force field,[29] were obtained by fitting the gas–phase electrostatic potentials of small peptides calculated by HF/6–31G* using the restrained electrostatic potential (RESP).[30] The potential in Eq. (8) does not allow reaction of peptide–H^+ and may only be used to study energy transfer in peptide–H^+ + surface collisions.

With the AM1, PM3, RM1, and MP2 QM models, fragmentations and reactions of peptide–H^+ were studied for two types of simulations, QM+MM and QM/MM. In the QM+MM model,[12,15-17,20] peptide–H^+ was represented by a QM model, but the interaction between peptide–H^+ and the surface was represented by a MM analytic potential energy function. This model allows for the study of fragmentation pathways for the collisionally excited peptide–H^+, but not the reactivity between the peptide and the surface. For this method, the surface potential and the peptide–H^+/surface potential are MM, but the peptide–H^+ potential is QM. There is no direct coupling between these potentials and each is separable.

To study reaction between peptide–H^+ and the surface, the QM/MM model is used. Within this model peptide–H^+ and a part of the surface must both be reactive, and hence described by a QM model, while the remainder of the surface is MM.[13] The QM peptide–H^+ interacts with the MM region of the surface via a MM model. A MM potential is required to "join" the QM and MM surface regions. This is called a QM/MM model,[13] since there is a coupled, chemical bonding, interface between the QM and MM components of the surface. Our QM+MM model is compared with a QM/MM model in ref.16.

C. $V_{surface,\ peptide}$

1. Non–reactive MM model

The non–reactive MM potential model for interaction between peptide–H^+ and the surface is given by a sum of two body–terms between the atoms of the surface and those of peptide–H^+;[11,31,32]

$$V_{surface,\ peptide} = \sum_i \sum_j \left\{ A_{ij} e^{-B_{ij} r_{ij}} + \frac{C_{ij}}{r_{ij}^n} + \frac{D_{ij}}{r_{ij}^m} \right\} \quad (9)$$

here i and j refer to atoms belonging to peptide–H^+ and the surface, and r_{ij} their interatomic distance. The $\frac{D_{ij}}{r_{ij}^m}$ term is included with the Buckingham potential to provide additional flexibility in the repulsive potential function. The n and m are integers, and A_{ij} and B_{ij} are positive. In the initial fits,[11,31] the D_{ij} term was not included, no constraint was enforced on the sign of C_{ij}, and n was either 6 or 5. Constraints were included in the most recent fit,[32] with C_{ij} and D_{ij} negative and positive numbers, respectively, $m - n \geq 3$, and the minimum value of n never less than 5. The complexity of Eq. (9) is required to accurately fit both the high energy repulsive and low energy attractive regions of the potential energy curves.

The parameters for the potential in Eq. (9) were derived from high level *ab initio* potential energy curves (IPECs).[11,31,32] To develop potentials between diamond and H–SAM surfaces and poly – glycine and –alanine ions, gly_n–H^+ and ala_n–H^+, the CH_4 molecule was used to model the H– and C–atoms of the surfaces and CH_4, NH_3, NH_4^+, H_2CO, and H_2O were used as models for the different types of atoms and functional groups comprising the peptides.[11] The IPECs were calculated for a range of orientations to sample all of the atom–atom interactions between the surface and peptide ions. These IPECs are then fit simultaneously to determine the parameters in Eq. (9). In fitting the IPECs, the focus was to accurately fit the short range repulsive region to study energy transfer and peptide–H^+ fragmentation upon collision with the

surfaces. A similar study was performed for $gly_n–H^+$ and $ala_n–H^+$ interactions with the F–SAM surface, using CF_4 as a model for the F– and C– atoms of the F–SAM.[31]

Both long–range attractive and short–range repulsive interactions were determined and fit for $CH_3NH_3^+$ interacting with CH_4, to compare with the above smaller NH_4^+/CH_4 system. The two–body repulsive interactions between CH_4 and the $–NH_3^+$ atoms of $CH_3NH_3^+$ and NH_4^+ are nearly identical, showing that the NH_4^+/CH_4 system accurately describes these interactions.[33]

In a recent computational study both short–range repulsive and long–range attractive potentials were accurately fit by Eq. (9) for $gly_n–H^+$ and $ala_n–H^+$ interacting with the F–SAM surface.[32] With the attractive potentials included soft landing may be studied in the collisions, in addition to collision energy transfer. The fitting was performed with a new genetic algorithm (GA),[34] which looks for a set of parameters that minimize a cost function written as a sum of weighted squared differences between the calculated and the reference (*ab initio*) interaction energies. The fits were controlled by imposing certain limits or constraints on the parameter values, in order to obtain reasonable pair potentials and avoid the Buckingham catastrophe at short distances. As above, CF_4 was used to represent the F–SAM. CH_4, NH_3, NH_4^+ were retained as models for the peptide ions' atoms and functional groups, but H_2CO and H_2O were replaced with HCOOH. The IPECs were calculated at the MP2/aug–cc–pVTZ level of theory. The calculated and fitted IPECs for CH_4/CF_4 are given in Figure 2. The two–body parameters for all of the fits are listed in Table 2 of ref. 32. The transferability of these parameters were tested by using them to calculate IPECs for CF_4 interacting with the $–NH_2$ group of $HCONH_2$ and then comparing them with curves calculated with MP2/aug–cc–pVTZ. This comparison is shown in Figure 3 and it is seen that the two sets of curves are in excellent agreement, illustrating the transferability of the potential parameters.

2. Reactive QM/MM model

To model reaction between peptide–H^+ and the surface, i.e. reactive landing, the surface potential must be modified to include a QM region within the surface.[13] The minimal model involves including the propyl tip of the center chain of the SAM in the QM region. The last carbon atom in this chain is treated as a capped linking atom[35] to complete the valence of the QM region. As reactive landing typically takes place with a chemically modified SAM, this center chain was also modified to a –(CO)Cl head–group where the chloride acts as a good leaving group during the reaction[13] as shown in Figure 1b. The interaction between any added head-group atoms and the rest of the surface must be defined. These terms are MM Buckingham terms that were obtained[13] using a similar approach to that described in Section II.C.1 to create the peptide-H^+/SAM interaction potential. Larger QM regions have also been used in which the eight chains surrounding the center chain are also included as a QM buffer.[13] The single chain model yields nearly identical results as those that include the QM buffer.[13] In future work it will be of interest to consider a broader range of sizes for the QM region of the surface.

III. Simulation Methodology

The classical trajectory chemical dynamics simulations were carried out with the general chemical dynamics package VENUS.[36] In a classical trajectory study the motion of individual atoms are simulated by solving the classical equations of motion in the form of either Hamilton's equations

$$\frac{\partial H}{\partial q_i} = \frac{-dp_i}{dt} \; and \; \frac{\partial H}{\partial p_i} = \frac{dq_i}{dt} \tag{10}$$

or Newton's equations

$$m_i \frac{d^2 q_i}{dt^2} = -\frac{\partial V(\mathbf{q})}{\partial q_i} \quad (11)$$

In these equations, H the Hamiltonian is the sum of the system's kinetic $T(\mathbf{p})$ and potential $V(\mathbf{q})$ energies, $H = T(\mathbf{p}) + V(\mathbf{q})$, $\mathbf{p}$'s are the momenta and $\mathbf{q}$'s the coordinates, $\partial H/\partial q_i = \partial V/\partial q_i$ the potential gradient for coordinate q_i, m_i the mass associated with coordinate q_i, and d^2q_i/dt^2 the acceleration. Cartesian coordinates and momenta are used to represent the energy, and for N atoms there are 3N of each.

An algorithm is required to numerically integrate the classical equations of motion for propagating the trajectory. Three different algorithms have been used; i.e. combined Runge–Kutta/Adams–Moulton, the symplectic velocity Verlet,[37] and a 6th–order symplectic integration scheme.[38] Tests are required to determine which algorithm is most efficient for the particular system under investigation.

When a trajectory is completed, the final values of momenta and coordinates are transformed into properties that can be compared with experiment and provide atomistic details regarding the peptide–H^+ + surface collision. The simulation provides information concerning the following: the final energy distribution for peptide-H^+ and the surface, and the energy remaining in peptide-H^+/surface relative translational motion; the angle at which peptide-H^+ scatters off the surface; and the probabilities and mechanisms for processes including, proton migration within peptide-H^+, peptide-H^+ fragmentation (i.e. SID), formation of complexes between peptide-H^+ fragments, covalent linkage to the surface (i.e. RL), and intact penetration/adsorption onto the surface (i.e. SL).

A. Trajectory initial conditions

A peptide–H^+ + surface chemical dynamics simulation requires choosing initial conditions for the ensemble of trajectories which are calculated. Initial conditions are chosen separately for peptide–H^+, the surface, and the conditions for the peptide–H^+ + surface collision. Each of these are discussed in the following.

1. Peptide ion

Vibrational and rotational energies are added to peptide–H^+ by quasiclassical normal mode sampling, as described by the following steps.[11,39]

1. Normal mode frequencies and eigenvectors for peptide–H^+ ion are determined by diagonalizing the ion's mass weighted Cartesian force constant matrix. The harmonic oscillator quantum–mechanical Boltzmann distribution is randomly sampled for each of the ions normal modes to select its vibrational quantum number n_i and energy $E_i^o = (n_i + ½)h\nu_i$. The ion is assumed to be a symmetric top and its angular momentum j and z component are determined by randomly sampling their classical Boltzmann distributions. The angular momentum components j_x and j_y are determine by randomly projecting j onto the xy plane. These random values of j_x, j_y, and j_z form the rotational angular momentum vector **j** for the ion and are used to calculate its rotational energy E_{rot}^o.

2. The energy of each normal mode, is expressed classically as $E_i^o = (P_i^2 + \omega_i^2 Q_i^2)/2$, where the P_i and Q_i are the normal mode momenta and coordinates. A random phase is chosen for each normal mode with energy E_i^o to determine its P_i and Q_i. The total energy for the peptide ion is the sum of its vibrational and rotational energies, $E^o = \sum_{i=1}^{3N-6} E_i^o + E_{rot}^o$. The normal mode **P** and **Q** are then transformed to Cartesian coordinates **p** and **q** using the normal mode eigenvector and equilibrium coordinates. Only momenta may be added to low frequency modes for which this transformation is inaccurate.[40]

3. A spurious angular momentum $\mathbf{j_s}$ arises from this transformation since normal modes are approximate for finite displacements. It is given by the expression $\boldsymbol{j_s} = \sum_{i=1}^{N} \boldsymbol{r_i} \times m_i \dot{\boldsymbol{r}}_{\boldsymbol{i}}$, where m_i and r_i are the mass and position vector of the ith atom. The desired angular momentum $\boldsymbol{j}$ is added to the peptide ion by forming the vector $\boldsymbol{j_a} = \boldsymbol{j} - \boldsymbol{j_s}$ and adding the rotational velocity $\boldsymbol{\omega} \times \boldsymbol{r_i}$ to each of the atoms, where $\boldsymbol{\omega} = \boldsymbol{I^{-1}} \boldsymbol{j_a}$ and $\boldsymbol{I^{-1}}$ is the inverse of inertia tensor.

4. The actual internal energy E chosen from steps 1–3, is calculated using the correct anharmonic Hamiltonian and compared with the intended energy E^o. If they do not agree within some acceptance criterion, the Cartesian coordinates and momenta are scaled by $(E^o/E)^{1/2}$. Any spurious center of mass translational energy is subtracted from the peptide, and the procedure loops back to step 3, until E is within the acceptance criterion of E^o. Then the selected coordinates **q** and momenta **p** of the peptide are saved.

5. The q's and p's selected for the peptide ion are then randomly rotated about the ion's Euler's angles to give the ion a random orientation.

2. Surface

A molecular dynamics (MD) simulation procedure was used to select random coordinates and momenta for the diamond and SAM surfaces. Initial conditions for the surfaces were chosen by first assigning velocities, chosen from a Maxwell–Boltzmann distribution at the desired surface temperature T_s (usually 300 K), to the surface atoms. The surface was then equilibrated for a fixed time (1 – 2 ps) by a MD trajectory simulation, with velocity rescaling, so that the surface temperature corresponds to the desired T_s. The simulation is then run for an additional fixed time, without velocity rescaling, to ensure equilibration. These final positions and momenta are used as the initial configuration for the trajectory simulation. This approach was used for each trajectory.

3. Sampling of peptide + surface relative properties

In the mass spectrometry experiments the peptide ions collide with the surface with collision energy E_i and incident angle θ_i with respect to the surface normal. To model these experiments a beam of peptide–H^+ ions is directed toward the surface.[41] These ions are randomly placed in a circular area of the beam, whose diameter was chosen so that it overlapped a unit cell on the surface. The azimuthal angle χ, between the beam and a fixed plane perpendicular to the surface, was sampled randomly between 0 to 2π to simulate collisions with different domains of growth on the surfaces. The distance between the center of beam and the top of the surface is set to a value large enough (e.g. 25 – 30 Å) so that the peptide–H^+ ions are not interacting with the surface when the trajectories are initiated.

IV. Simulation Dynamics and Comparisons with Experiment

In the following, results of the peptide-H^+ + surface simulations are presented and compared with experiment. Collisional energy transfer, peptide-H^+ fragmentation, SL, and RL are considered for different peptide-H^+ ions, H-SAM, F-SAM, and diamond surfaces, and for a range of collision energies E_i and incident angles θ_i. Representative atomistic animations of the simulations discussed in the following are on the web portal http://hase-group.ttu.edu.

A. Collisional energy transfer

Experimental measurements of the percentage energy transfer to the peptide-H^+ ion's vibrational/rotational degrees of freedom, ΔE_{int}, have been performed for several systems: ala_2–H^+ + F–SAM ($\theta_i = 0^o$ and $E_i = 5 – 23$ eV, $\Delta E_{int} = 21\%$);[42] des–Arg^1–bradykinin ($\theta_i = 0^o$ and $E_i = 5 – 23$ eV)[43] colliding with the H–SAM ($\Delta E_{int} = 10\%$), LiF ($\Delta E_{int} = 12\%$), diamond ($\Delta E_{int} = 19\%$), and F–SAM surfaces ($\Delta E_{int} = 20.5\%$). The energy transfer distribution widths varied

according to H–SAM < F–SAM < LiF < diamond. An interesting finding from these experiments is that the percentage energy transfer to ΔE_{int}, for collision with the F–SAM, is nearly the same for $ala_2–H^+$ and the much larger ion des–Arg^1–bradykinin.

Chemical dynamics simulations were performed to study $gly_n–H^+$ and $ala_n–H^+$ collisional energy transfer efficiencies as a function of the surface, the peptide–H^+ size and structure, the intramolecular potential used for $V_{peptide}$, and the incident energy E_i and angle θ_i. When comparisons can be made, the simulation results are in quite good agreement with the above experimental findings of Laskin, Futrell, and co–workers.[42,43] The specific comparison made is for the efficiency of collisional energy transfer to ΔE_{int}.

1. H-SAM and diamond surfaces

A simulation study was performed for $gly_3–H^+$ and $gly_5–H^+$ using AMBER for $V_{peptide}$.[11] Results for $gly_3–H^+$ colliding with the H–SAM and diamond surfaces are summarized in Table 1, for E_i = 30 eV and $\theta_i = 45^o$. Both folded and extended, beta–sheet type structures are considered, and the structures give similar percentage transfers to ΔE_{int}. However, for collisions with the H–SAM, the folded structure transfers more energy to the surface, ΔE_{surf}, than retaining in translation, E_f. The larger folded $gly_5–H^+$ ion gives ΔE_{int}, ΔE_{surf}, and E_f energy transfer percentages of 23, 5, and 72%, respectively, for collision with diamond and percentages similar to those for $gly_3–H^+$. Energy transfers to ΔE_{int}, for the $gly_3–H^+$ and $gly_5–H^+$ ions, agree with the above H–SAM and diamond experimental results for des–Arg^1–bradykinin. A more direct comparison with the des–Arg^1–bradykinin + H–SAM experiment[43] is from a $gly_8–H^+$ + H–SAM simulation at $\theta_i = 0^o$ and using PM3 for $V_{peptide}$, for which energy transfer to ΔE_{int} is 11.9%.[20]

The effect of the incident angle on energy transfer was studied, for the $gly_8–H^+$ + H–SAM[20] collisions, by changing θ_i from 0^o to 45^o. This change had only a small effect on the

transfer to ΔE_{int}, but decreased the transfer to ΔE_{surf}. The H-SAM surface is highly corrugated, with substantial roughness, and the 0^o and 45^o incident angles may have similar energy transfer dynamics for ΔE_{int}.

For simulations of $gly_8–H^+$ colliding with the diamond surface,[18] agreement is not obtained with the des–Arg^1–bradykinin + diamond experiments.[43] However, there is some uncertainty whether the surfaces used for the simulations and experiments are the same. For the experiments, the percentage energy transfer to ΔE_{int} is 19% for $\theta_i = 0^o$. But for this θ_i, the simulations give 45, 26, and 29% for the ΔE_{int}, ΔE_{surf}, and E_f energy transfer percentages, respectively. In contrast, for $\theta_i = 45^o$, these respective energy transfer percentages are 26, 12, and 62%. The $\theta_i = 0^o$ and 45^o energy transfer percentages are approximately a factor of two different, consistent with $\cos^2\theta_i$ scaling.

The 26% energy transfer to ΔE_{int} at 45^o is in approximate agreement with the experimental value of 19% and may be more representative of the experimental study than the simulation percentage of 45% at 0^o. In contrast to the perfectly "flat" diamond surface used for the simulations, the surface used in the experiments is inherently "rough".[43] The experimental diamond surface is grown by "merging" of different nucleation sites. In addition, there is an unknown much softer graphitic fraction of carbon on the surface.[18] It is expected that a perfectly flat diamond surface transfers substantially more energy to the peptide–H^+ vibrational modes than does a rough and partially graphitic diamond–like surface. Non–normal collisions with an incident angle of 45^o may approximate surface roughness effects.

2. F-SAM surface

For simulations of $ala_2–H^+$ colliding with the F–SAM surface, excellent agreement with experiment is found for both the average energy transfer to ΔE_{int} and its distribution.[14] For $\theta_i = 0^o$

and E_i = 5 – 23 eV, as in the experiments, the average percentage energy transfer to ΔE_{int} ranges from18 – 20%, similar to the experimental value of 21%. As shown in Figure 4, the distribution of energy transfer to ΔE_{int} is also in quite good agreement with experiment.

The effect of the incident angle on the ala_2–H^+ + F–SAM energy transfer was studied by changing θ_i from 0^o to 45^o.[14] As found above for the gly_8-H^+ + H-SAM simulation, this change had only a small effect on the transfer to ΔE_{int}, but decreased the transfer to ΔE_{surf}. The SAM surfaces are highly corrugated, with substantial roughness, and the 0^o and 45^o incident angles may have similar energy transfer dynamics for ΔE_{int}. These dynamics may result from the inherent roughness of the H-SAM and F-SAM surfaces.

A detailed analysis was made of the different trajectory types for the ala_2-H^+ + F-SAM simulations[44] and their energy transfer percentages. As shown in Table 2, four different trajectory types were identified; i.e. directly scattered, temporarily only physisorb, temporarily only penetrate/physisorb, and trapped at the termination of the 10 ps trajectories. Temporarily only physisorb is important at low collision energies, while all the trajectories directly scatter at a high collision energy. Temporarily only penetrate/physisorb events are important at intermediate collision energies. Rather remarkably, the energy transfer percentages are overall insensitive to the trajectory type.[44] It will be important to see if these dynamics are found for other peptide-H^+ + surface collisions.

3. Effect of the $V_{peptide}$ potential

A possible effect regarding the nature of $V_{peptide}$ on energy transfer was studied for gly–H^+ collisions with diamond at E_i = 70 eV and $\theta_i = 45^o$. In these studies, $V_{peptide}$ was treated using the AMBER MM model,[12] and the QM models AM1[12] and MP2/6–31G*.[17] As shown in Table 3, they give statistically the same average energy transfer efficiencies. The same type of agreement

is found in comparing the AMBER[15] and AM1[16] energy transfer efficiencies for $gly_2–H^+$ + diamond collisions at E_i = 70 eV and θ_i of 0° and 45°. The AMBER and AM1 distribution for ΔE_{int}, ΔE_{surf}, and E_f are compared in Figure 5 and they are the same within statistical uncertainties. From these studies, we conclude that the energy transfer is insensitive to the treatment of $V_{peptide}$.

B. Peptide–H^+ fragmentation

1. IVR and shattering fragmentation

If a sufficient fraction of the peptide–H^+ collision energy is transferred to the ion's vibrational degrees of freedom, the ion will fragment providing important information regarding the ion's fragmentation pathways and fragmentation energetics. This process is called SID and the fragmentation ions detected for peptide–H^+ ion may be used to determine the peptide's primary structure.

The traditional fragmentation mechanism is described by the Rice–Ramsperger–Kassel–Marcus (RRKM) model[45] in which the peptide ion is activated by its collision with the surface, "bounces off", and then dissociates after undergoing efficient intramolecular vibrational energy redistribution (IVR). However, first from simulations[12,46] and then from experiments[47] a "shattering" mechanism was also identified in which the ion fragments as it collides with the surface. Shattering is non–RRKM fragmentation and is the origin of the large increase in number of product channels with increase in E_i.[16,47] Many of these channels have high unimolecular thresholds and only occur as a result of the non–statistical dynamics of shattering. Shattering becomes the dominant dissociation mechanism at high E_i.

Table 4 gives the results of a QM+MM simulation, using AM1, for $gly_2–H^+$ collisions with diamond for E_i of 30 to 100 eV and θ_i = 0°.[16] The fraction of the total number of trajectories

which shatter increases dramatically from 0.08 to 0.71 as E_i is increased from 30 to 100 eV. This is accompanied by a large increase in the number of fragmentation pathways from 6 to 59.

The importance of shattering was compared for AM1 and MP2/6–31G* QM+MM simulations of gly–H^+ collisions with diamond at E_i = 70 eV and $\theta_i = 45^o$.[17] The fraction of the total number of trajectories which shatter is 0.23 and 0.22 for AM1 and MP2, respectively, and their respective numbers of fragmentation pathways are 18 and 14. The fragmentation pathway with the lowest potential energy barrier, i.e. $NH_2CH_2^+ + CO + H_2O$, is not observed by either the AM1 or MP2 simulation. The MP2 simulation at E_i = 70 eV was also performed for $\theta_i = 0^o$, instead of 45^o, and the fraction of the trajectories which shatter increased to 0.57 with 96 fragmentation channels. For comparison the AM1 simulation for gly_2–H^+, at the same E_i = 70 eV and $\theta_i = 0^o$, has a shattering fraction of 0.44 and 44 fragmentation channels.

Shattering is important for the large ion gly_8–H^+ colliding with the diamond surface for E_i = 100 eV and θ_i of 0^o and 45^o.[18] The fraction of the trajectories which shattered is 0.78 and 0.22 for θ_i of 0^o and 45^o, respectively. For the $\theta_i = 0^o$ simulation, the number of fragmentation pathways is quite large and 304, with many related by their backbone cleavage patterns.

Shattering does not occur for gly_8–H^+ collisions with the H–SAM for E_i of 5 to 110 eV and θ_i of 0^o and 45^o,[20] but is important for gly_2–H^+ collisions with chemically modified F–SAM surfaces.[13] The F–SAM surface was modified by substituting a –COCl or –CHO head group on the terminal carbon of a single chain of the SAM. This modification was done for a chain in the middle of the F–SAM model as shown in Figure 1b. The simulations are QM/MM so that gly_2–H^+ may react with surface. For this CHO–SAM the fraction of peptide fragmentation, without reaction with the surface, which is shattering increases from 0.05 to 0.21 as E_i is increased from 10 to 55 eV. For the COCl–SAM this increase is larger and from 0.05 to 0.36.

2. Atomistic fragmentation mechanisms

Fragmentation also occurs due to proton migration within peptide-H^+. Experimentalists have developed the empirical "mobile proton model" to describe fragmentation of peptide ions in the gas phase induced by vibrational excitation. This model provides a qualitative framework to think about proton-driven SID and has been recently reviewed.[48] Within this model, prior to collision with the surface, the peptide's excess proton is localized at the most basic site. The energy transfer that takes place during the collision is then thought of as a gradual "heating" of the peptide which mobilizes the excess proton. As the proton migrates to thermodynamically less stable sites, particular covalent bonds along the peptide backbone are weakened, which in turn leads to fragmentation. Barnes and co-workers have used chemical dynamics to study SID and proton migration in the gly_8–H^+ + F–SAM collision system.[49,50] The dynamics observed by these simulations are in good agreement with the mobile proton model. In addition, the dynamics revealed that following the initial fragmentation event, the peptide fragments may associate with each other to form complexes. This is an important finding since it means that the excess proton is not carried away by a fragment during the first fragmentation event, but rather remains within the complex and can participate in secondary fragmentations. The simulations illustrate fragmentation products that result from secondary fragmentation events that would not be possible in the absence of a complex.

These atomistic mechanism dynamics by Barnes and co-workers are complemented by similar studies for fragmentation of gly-H^+,[12,17] gly_2-H^+,[16] and gly_8-H^+[18] in collisions with the diamond {111} surface. The fragmentation pathways promoted by both the IVR and shattering mechanisms are identified, as well as the first backbone site to fragment in the dissociation.

Detailed mechanistic analyses were made for the gly_8-H^+ fragmentations. Following typical mass spectrometry studies, the dominant backbone cleavages were a-x and b-y, and most promoted by shattering. Rearrangement of the dissociation fragments was observed, as well as association of the fragments, leading to products not characterized by the peptide-H^+ primary structure, as found by Barnes and co-workers.[49,50] The formation of complexes by association of the peptide fragments has been described in the literature. The work described here is the first to observe it in trajectory simulations.

Barnes and co-workers have also recently investigated the small, lysine containing model peptide, GGKG-H^+ with a focus on how conformation and protonation site affect peptide-H^+ fragmentation mechanisms.[51] The inclusion of lysine is an important extension of the studies of the protonated polyglycine and polyanaline systems as it allows for the important possibility of side-chain protonation. It is known from experiment that as the basic nature of the side-chain increases, the fragmentation efficiency decreases,[52] making the simulation of a peptide with a basic side-chain of interest.

In their study, simulations were performed for five different conformation/protonation site combinations that examined both side-chain and backbone protonation at the N-terminus, which are referred to as SC and BB protonation, respectively. Three striking results were revealed in this work. First, the initial conformation of a peptide can have a dramatic effect on proton mobility pathways. This was highlighted by examining the differences seen between two SC protonated conformers, one with lysine hydrogen bonded to the N-terminus and the second with it hydrogen bonded to the C-terminus. The excess proton was more likely to migrate to the side of the peptide involved in the initial hydrogen bond. Secondly, it was found that SC protonation of lysine results in a dramatic increase in "charge-remote" (i.e. not proton-driven)

fragmentation events compared to BB protonation. For example, for the same conformational family at a collision energy of 70 eV, 91% of fragmentation events are charge-remote for SC protonation, while just 27% of BB protonation fragment through a charge-remote mechanism within the time frame of the simulation. Lastly, it was found that BB protonation yields the same mobile-proton driven mechanism as that found in polyglycine systems, like octaglycine. This was revealed through the use of a new technique to depict proton mobility termed "proton hop probability maps," which can be used to visually illustrate how likely a given proton migration pathways is on a hop-by-hop basis or for the hop preceding fragmentation.

C. Soft–landing

When peptide-H^+ collides with a surface and adheres to it without the formation of a covalent bond, it is said to be trapped via a SL process.[6,7,10] SL was observed in a very recent simulation study of ala_2–H^+ + F–SAM collisions,[14] that used a newly developed $V_{surface,\ peptide}$ potential[32] that includes accurate attractive interactions. The F-SAM consists of CF_3-$(CF_2)_7$-S- perfluorinated chains. The relatively low collision energies of E_i = 5.0 and 13.5 eV, with an incident angle 0^o to the surface normal, were found to be most effective for SL with ala_2–H^+ trapping percentages of 84% and 65%, respectively. The simulations show the trapping probability decreases with increase in incident angle. For E_i = 22.5 eV, it decreases from 41 to 6% for change in the incident angle from 0 to 45^o.

Adsorption of ala_2–H^+ on the F–SAM surface is a complex process, since the ion interacts with the surface via multiple interaction terms.[32] The overall strength of the ala_2–H^+ interaction with the surface is substantially higher than the peptide's thermal translational energy. The composite of the interactions gives the structure for the ion binding with the surface, as well as its binding energy. From a MD simulation study, structures have been found for ala_2–

H^+ binding with the F–SAM surface, as illustrated in Figure 6. The resulting binding energies were ~ 10–15 kcal/mol. Binding occurred by penetration of the ion between the chains of the surface. Furthermore, as a result of these peptide/surface interactions, adsorption of the peptide is expected to strongly influence the peptide's shape and size. Analyses of the radius of gyration of trapped ala_2–H^+ have shown less compactness as compared to the optimized ala_2–H^+ structure.[44] The structure of the trapped ion becomes less compact by breaking a hydrogen bond between the –OH and –NH– groups. Trapping of ala_2-H^+ on/in the F-SAM decreases its compactness.

In a very recent study[44] it was found that trapping (SL) of ala_2–H^+ on the CF_3-$(CF_2)_7$-S-F–SAM is predominantly a multi–step process. The following were identified as mechanisms for adsorption followed by trapping on the F–SAM: (i) physisorption–penetration–physisorption (phys-pen-phys); (ii) penetration–physisorption–penetration (pen-phys-pen); (iii) penetration–physisorption (pen-phys); (iv) physisorption–penetration (phys-pen); and (v) only physisorption (phys). The fractions of the trajectories which followed these mechanisms are listed in Table 5 for E_i of 5 and 13.5 eV with θ_i of 0^o. To clarify these mechanism identifiers, "phys-pen-phys" means that ala_2-H^+ first physisorbs on the F-SAM, then penetrates the surface, and is then physisorbed when the trajectory is terminated. For the 5 eV simulations, 84% of the ala_2-H^+ ions are trapped, with 40% first penetrating the surface and 44% first physisorbing on the surface. The pen-phys-pen, pen-phys, phys-pen, and phys mechanisms have similar probabilities. At 13.5 eV, 65% of the trajectories are trapped, with 47% first penetrating and only 18% first physisorbing. Pen-phys is the dominant trapping mechanism.

Analyses were performed, for the $\theta_i = 0^o$ and E_i of 5 and 13.5 eV trajectories, to determine the average fraction of the ala_2-H^+ which penetrate the F-SAM surface (f_{pen}) for the events where ala_2-H^+ is trapped on/in the F-SAM at the conclusion of the trajectories. Figure 7

presents the distribution of f_{pen}. For both E_i of 5 and 13.5 eV the most probable f_{pen} is between 0.9 and 1.0 and the average value is 0.7. For these two E_i most of the penetration is near the top of the CF_3-$(CF_2)_7$-S- chains.

D. Reactive–landing

RL has been modeled for gly_2–H^+ reacting with both an F–SAM[13] and H–SAM[53] surface chemically modified to include a –COCl head group, as depicted in Figure 1b. The F–SAM also considered a –CHO head group, as described above in our discussion of shattering. These simulations were designed to provide insight into the experiments of Wang and Laskin,[54] in which a cyclic, lysine containing pentapeptide collided with a SAM of *N*–hydroxysuccinimidyl (NHS) ester–terminated alkylthiol on gold, which has been termed the NHS–SAM. The NHS head group is a good leaving group, but too large to add into the QM calculation, hence in these simulations it was modeled by a chlorine atom. Experimentally it was determined that the reactive landing took place at the nitrogen of the lysine side chain, and had a strong collision energy dependence, quickly peaking at a collision energy of 40 eV before dropping off. Although gly_2–H^+ does not have a lysine side chain, there are several reactive landing sites within the peptide.

In the simulations, RL on the COCl–SAM proceeds through a four–center transition state involving the carbonyl carbon of the surface, the chlorine atom, and two atoms from the peptide.[13] Most frequently, one of these peptide atoms is a hydrogen, but it is possible for RL and peptide fragmentation to occur within the same trajectory, hence a (peptide fragment)–Cl adduct is possible. RL shows a strong collision energy dependence, both experimentally and within the

simulations. As the collision energy increases, RL must compete with many other product pathways, including intact surface deposition, peptide–fragment deposition, and SID. The number of independent product pathways grows quickly with collision energy, however, the one most directly comparable to experiment is intact surface deposition. In this product pathway the peptide is covalent linked to the SAM surface while maintaining an intact heavy atom framework, i.e. fragmentation does not occur. During this process the leaving group evolves with a hydrogen to form HCl within the simulations or H–NHS in the experiments. Qualitatively similar collision energy dependent profiles are observed for intact surface deposition in the simulations and the RL efficiency in experiment. In order to test the effect of the leaving group, the CHO–SAM was also simulated.[13] It was found that the probability for surface deposition decreased by approximately a factor of two.

Both the H and F–SAM with a –COCl head group have been simulated,[13,53] and both proceed through the four–center transition state described above. The largest difference between the two systems is the overall reactive fraction. The modified F–SAM is five times more reactive than the modified H–SAM. The stiffness of the surface plays a large role in this result. In the F–SAM system the two surface atoms involved in the four atom transition state are held in place, which results in a larger reactive fraction.

V. Conclusions

Classical trajectory chemical dynamics simulations give good agreement with experiment regarding the dynamics of peptide–H^+ collisions with organic surfaces. Comparisons between simulation and experiment are made for the energy transfer and peptide–H^+ fragmentation of SID, and the efficiencies and mechanisms of SL and RL. The methodology of the simulations is

well understood and software is available for performing this type of simulations. Accurate peptide-H^+ intramolecular, peptide-H^+/surface intermolecular, and surface potentials are required to perform these simulations, and significant effort has been undertaken to develop such potentials. In addition, the appropriate model (MM, QM+MM, or QM/MM) for the potential must be selected depending on the process one wishes to study.

The collisions of peptide-H^+ ions with organic surfaces include a wide variety of physical and chemical processes as described above, with particular interest in SID, SL, and RL. The chemical dynamics simulations provide important information concerning: collision energy transfer to the internal energy of peptide-H^+ and to the surface; probabilities and mechanisms for SL, proton migration within peptide-H^+, peptide-H^+ fragmentation, and formation of complexes between the fragments. Important information may be extracted from the translational energies and internal energies of the scattered ions and fragments. The penetration depth of peptide-H^+ during the collision may be related to the ion/surface interaction time, collision energy, and nature of the peptide-H^+ and surface. This dynamical information may be compared with peptide-H^+/organic surface scattering experimental data, such as the change in the internal energy of the projectile, upon collision with the surface. Atomistic motions obtained from the simulations provide insight into the mechanisms for SL, RL, and SID, such as shattering. The combined efforts of experimentalists and computational/theoretical scientists help enrich the knowledge and hence a better understanding of the dynamics associated with collisions of peptide-H^+ ions with organic surfaces.

Though extensive atomistic details concerning the dynamics of peptide–H^+ + surface collisions, with detailed comparisons with experiments, have been obtained, there remain multiple avenues of investigation for future studies. The following are some inquiries to pursue

regarding energy transfer, fragmentation, SL and RL. Perplexing questions remain concerning the energy transfer efficiencies to the peptide–H^+ internal degree of freedom ΔE_{int} to the surface ΔE_{surf}, and the amount remaining in peptide–H^+ translation E_f. For collisions with the H–SAM and F–SAM surfaces the percentage energy transfer to ΔE_{int} is independent of the collision energy E_i, while the transfers to ΔE_{surf} and E_f increase and decrease, respectively, with increase in E_i. Upon changing the incident angle θ_i from normal, 0^o to 45^o, there is negligible change in the transfer to ΔE_{int}, while the transfer to ΔE_{surf} and E_f decrease and increase, respectively. In addition, the percentage transfer to ΔE_{int} is apparently insensitive to peptide–H^+ size, since it is the same for ala_2–H^+, gly_8–H^+, and protonated des–Arg^1–bradykinin.

The energy transfer dynamics are quite different for collisions with the diamond {111} surface. As for the SAM surfaces, percentage energy transfer to ΔE_{surf} and E_f increases and decreases, respectively, with increase in E_i, but the percentage energy transfer to ΔE_{int} is somewhat dependent on E_i. All the energy transfers depend on θ_i and all approximately scale according to $cos^2\theta_i$. Finally, the percentage energy transfer to ΔE_{int} increases as the size of peptide–H^+ increases, contrary to the result for the SAM surfaces. A particularly vexing question is the different distributions of ΔE_{int} for the two surface types. The percentage energy transfer to ΔE_{int} is the same, for collisions with the F–SAM and diamond {111} surfaces, but the distribution for transfer to ΔE_{int} is substantially broader for the diamond surface. The distribution is similarly narrower for the H–SAM surface than for diamond.

More work needs to be done to determine from the simulation, the complete mass spectrum for the SID fragmentation of peptide–H^+. Shattering fragmentation forms product ions within the integration time of the classical trajectories, but some of these products have sufficient vibrational energy to undergo further unimolecular dissociation and their dissociations must be

accounted for in forming the mass spectrum. Some of the peptide–H^+ ions, which are vibrationally excited due to collision but do not shatter, dissociate during the trajectory integration time. As above, further dissociation of any of the product ions must be considered, in addition to the possibility of complicated reaction schemes due to complexation between peptide fragments. Also, many of the peptide–H^+ ions, which do not dissociate during the trajectory integration time, have sufficient vibrational energy to dissociate and must be accounted for. A straightforward approach for modeling the dissociation of the above vibrationally excited ions is to use RRKM theory. The vibrational energy distribution for each of the ions may be determined from the simulations, which are required for the RRKM calculations. A substantial effort that will be required is to "build" a database of the transition state structures, barrier heights, and vibrational frequencies for the ions' unimolecular decomposition pathways, information needed for the RRKM calculations.

More simulations studies of SL are needed. The only system studied is ala_2–H^+ colliding with F–SAM. Larger ions need to be studied, with a range of amino acids. Of interest is how the SL probability and mechanism(s), and structure of the adsorbed ion, depend on the size of the ion and its amino acid constituents. Direct comparisons with experiment are important. The same issues as above for SL pertain to RL. Of particular importance is the need to make direct comparison with experiment. This will be computationally challenging, but possible.

In concluding, the reported simulations have provided much important information regarding the dynamics of peptide–H^+ collisions with organic surfaces. However, there are multiple opportunities for both new and expanded studies. An important avenue for future efforts is to integrate the atomistic SID simulations discussed here with those for collision-induced dissociation (CID) of biological ions.[55] For CID, IVR and shattering mechanisms are identified

as discussed here for SID. It will be of both interest and importance to identify possible differences and similarities in the SID and CID fragmentations of peptide-H^+ ions.

Acknowledgments: The research reported here is based upon work supported by the Robert A. Welch Foundation under grant No. D–0005 and the National Science Foundation under grant CHE–1416428. Authors are particularly grateful for valuable discussions with J. Laskin, and S. A. Vázquez.

References

1. J. C. Love, L. A. Estroff, J. K. Kriebel, R. G. Nuzzo and G. M. M. Whitesides, *Chem. Rev*. 2005, **105**, 1103
2. J. C. Angus, Y. Wang and M. Sunkara, *Annu. Rev. Mater. Sci.* 1991, **21**, 221
3. V. Grill, J. Shen, C. Evans and R. G. Cooks, *Rev. Scientif. Instrum.* 2001, **72**, 3149–3179.
4. V. H. Wysocki, C. M. Jones, A. S. Galhena and A. E. Blackwell, *J. Am. Soc. Mass Spectrom.* 2008, **19**, 903–913.
5. P. Wang, O. Hadjar, and J. Laskin, *J. Am. Chem. Soc.* 2007, **129**, 8682–8683.
6. B. Gologan, Z. Takats, J. Alvarez, J. M. Wiseman, N. Talaty, Z. Ouyang and R. G. Cooks, *J. Am. Soc. Mass Spectrom.*, 2004, **15**, 1874–1884.
7. M. Volny, W. T. Elam, B. D. Ratner and F. Turecek, *Anal. Chem*., 2005, **77**, 4846–4853.
8. A. R. Dongre, A. Somogyi and V. H. Wysocki, *J. Mass Spectrom.* 1996, **31**, 339–350.
9. T. Pradeep, B. Feng, T. Ast, S. J. Patrick, R. G. Cooks and S. J. Pachuta, *J. Am. Soc. Mass Spectrom.* 1995, **6,** 187–194.
10. S. A. Miller, H. Luo, S. J. Pachuta and R. G. Cooks, *Science*, 1997, **275**, 1447
11. O. Meroueh and W. L. Hase, *J. Am. Chem. Soc.* 2002, **124**, 1524–1531.
12. S. O. Meroueh, Y. Wang, and W. L. Hase, *J. Phys. Chem. A* 2002, **106**, 9983–9992.
13. G. L. Barnes, K. Young, L. Yang and W. L. Hase, *J. Chem. Phys.* 2011, **134**, 094106.
14. S. Pratihar, S. C. Kohale, D. G. Bhakta, J. Laskin and W. L. Hase, *Phys. Chem. Chem. Phys.* 2014, **16**, 23769–23778.
15. J. Wang, S. O. Meroueh, Y. Wang, and W. L. Hase, *Int. J. Mass. Spectrom.* 2003, **230**, 57–64.
16. Y. Wang, W. L. Hase, and K. Song, *J. Am. Soc. Mass. Spectrom.* 2003, **14**, 1402–1412.

17. K. Park, K. Song, and W. L. Hase, *Int. J. Mass. Spectrom.* 2007, **265**, 326–336.

18. K. Park, B. Deb, K. Song, and W. L. Hase, *J. Am. Soc. Mass. Spectrom.* 2009, **20**, 939–948.

19. K. C. Hass, M. A. Tamor, T. R. Anthony, W. F. Banholzer, *Phys. Rev. B* 1992, **45**, 7171–7182.

20. G. L. Barnes and W. L. Hase, *J. Am. Chem. Soc.* 2009, **131**, 17185–17193.

21. L. Yang, O. A. Mazyar, U. Lourderaj, J. Wang, M. T. Rodgers, E. Martĭnez–Núñez, S. V. Addepalli and W. L. Hase, *J. Phys. Chem. C* 2008, **112**, 9377–9386.

22. W. Mar and M. L. Klein, *Langmuir*. 1994, **10**, 188–196.

23. J. Hautman and M. L. Klein, *J. Chem. Phys.* 1989, **91**, 4994– 5001.

24. O. Borodin, G. D. Smith and D. Bedrov, *J. Phys. Chem. B* 2002, **106**, 9912–9922.

25. M. D. Porter, T. B. Bright, D. L. Allara, and C. E. D. Chidsey, *J. Am. Chem. Soc.* 1987, **109**, 3559–3568.

26. G. Liu, P. Fenter, C. E. D. Chidsay, D. F. Ogletree, P. Eisenberger and M. Salmeron, *J. Chem. Phys.* 1994, **101**, 4301–4306.

27. H. Sellers, A. Ulman, Y. Shnidman and J. E. Eilers, *J. Am. Chem. Soc.* 1993, **115**, 9389–9401.

28. T. Yan and W. L. Hase, *J. Phys. Chem. B.* 2002, **106**, 8029–8037.

29. W. D. Cornell, P. Cieplak, C. I. Bayley, R. Gould, K. M. Merz, D. M. Ferguson, D. C. Spellmeyer, T. Fox, J. W. Caldwell and P. A. Kollman, *J. Am. Chem. Soc*. 1995, **117**, 5179–5197.

30. C. I. Bayly, P. Cieplak, W. D. Cornell, and P. A. Kollman, *J. Phys. Chem.* 1993, **97**, 10269–10280.

31. J. Wang and W. L. Hase, *J. Phys. Chem. B* 2005, **109**, 8320–8324.

32. S. Pratihar, S. C. Kohale, S. A. Vazquez, and W. L. Hase, *J. Phys. Chem B*. 2014, **118**, 5577–5588.

33. B. Deb, W. Hu, K. Song and W. L. Hase, *Phys. Chem. Chem. Phys*. 2008, **10**, 4565–4572.

34. J. M. C. Marques, F. V. Prudente, and F. B. Pereira, *J. Phys. B: At. Mol. Opt. Phys*. 2008, **41**, 085103.

35. A. Warshel and M. Levitt, *J. Mol. Biol.* 1976, **103**, 227–249.

36. X. Hu, W. L. Hase and T. Pirraglia, *J. Comput. Chem.* 1991, **12**, 1014–1024.

37. L. Verlet, *Phys. Rev.* 1967, **159**, 98–103

38. C. Schlier and A. Seiter, *Comput. Phys. Commum.* 2000, **130**, 176–189.

39. G. H. Peslherbe, H. Wang and W. L. Hase, *Adv. Chem. Phys.* 1999, **105**, 171–201.

40. U. Lourderaj, J. L. McAfee and W. L. Hase, *J. Chem. Phys.* 2008, **129**, 094701

41. S. B. M. Bosio and W. L. Hase, *J. Chem. Phys.* 1997, **107**, 9677–9686.

42. J. Laskin, E. Denisov and J. Furtell, *J. Am. Chem. Soc*. 2000, **122**, 9703–9714

43. J. Laskin and J. H. Furtell, *J. Chem. Phys*. 2003, **119**, 3413–3420.

44. S. Pratihar, N. Kim, S. C. Kohale, and W. L. Hase, *Phys. Chem. Chem. Phys.* 2015, **17**, 24576-24586.

45. T. Baer and W. L. Hase, *Unimolecular Reaction Dynamics. Theory and Experiments*, Oxford, New York, 1996

46. D. G. Schultz and L. Hanley, *J. Chem. Phys*. 1998, **109**, 10976–10983.

47. J. Laskin, T. H. Bailey and J. H. Futrell, *J. Am. Chem. Soc*. 2003, **125**, 1625–1632.

48. V. H. Wysocki, G. Tsaprailis, L. L. Smith, and L. A. Breci, *J. Mass Spectrom.* 2000, **35**, 1399-1406.

49. W. Ijaz, Z. Gregg and G. L. Barnes, *J. Phys. Chem. Lett.* 2013, **4**, 3935−3939.

50. Z. Gregg, W. Ijaz and G. L. Barnes, *J. Phys. Chem C* 2014, **118**, 22149-22155.

51. K. Shaikh, J. Blackwood, and G. L. Barnes, *Chem. Phys. Lett.* 2015, **637**, 83-87.

52. C. Gu, A. Somogyi, V. Wysocki, and K. F. Medzihradszky, *Anal. Chim. Acta* 1999, **397**, 247-256.

53. A. Geragotelis and G. Barnes, *J. Phys. Chem. C* 2013, **117**, 13087–13093.

54. P. Wang, O. Hadjar, P. L. Gassman and J. Laskin, *Phys. Chem. Chem. Phys.* 2008, **10**, 1512–1522.

55. D. Ortiz, J.-Y. Salpin, K. Song, and R. Spezia, *Int. J. Mass Spectrom.* 2014, **358**, 25-35.

Table 1. Comparison of Average Percentage Energy Transferred to Peptide Internal Energy, Surface Vibrations, and Peptide Translation for Folded and Extended gly_3–H^+ Collisions with Diamond {111} and H–SAM Surfaces[a]

	Diamond		H–SAM	
	Folded	Extended	Folded	Extended
ΔE_{int}	18	20	7	8
ΔE_{int}	9	8	63	54
E_f	73	72	30	38

a. E_i = 30 eV and $\theta_i = 45^o$.

Table 2. Percentages of Different ala_2-H^+ + F-SAM Trajectory Types

E_i (eV)	θ_i	Directly scatter[a]	Temporarily only physisorb[b]	Temporarily penetrate/physisorb[c]	Trapped[d]
5	0	12 ± 2	4 ± 1	0	84 ± 2
	45	13 ± 2	18 ± 2	0	69 ± 2
13.5	0	29 ± 2	4 ± 1	2 ± 1	65 ± 2
22.5	0	40 ± 2	4 ± 1	15 ± 2	41 ± 2
	45	82 ± 2	6 ± 1	6 ± 1	6 ± 1
30	0	57 ± 3	1 ± 0.5	13 ± 2	29 ± 2
70	0	100	0	0	0

a. ala_2-H^+ directly scatters from F-SAM
b. ala_2-H^+ temporarily physisorbs on the F-SAM without penetration
c. ala_2-H^+ temporarily penetrates the F-SAM with physisorption
d. ala_2-H^+ is trapped on/in the F-SAM at the conclusion of the 10 ps trajectories.

Table 3. Comparison of Energy Transfer Efficiencies Determined Using AMBER, AM1, and MP2/6–31G* Intramolecular Potentials for gly–H^+ Collisions with Diamond {111} with E_i = 70 eV and $\theta_i = 45^o$.

	Percentage Energy Transfer		
$V_{peptide}$	ΔE_{int}	ΔE_{surf}	E_f
AMBER	11	37	52
AM1	12	38	50
MP2	12	38	50

Table 4. Shattering Fraction versus Collision Energy for $gly_2–H^+$ + Diamond {111}.[a]

Collision Energy (eV)	Shattering Fraction	Number of Pathways
30	0.08	6
50	0.13	23
70	0.44	44
100	0.71	59

a. The collision angle is 0^o, perpendicular to the surface. The trajectories are QM+MM, with the AM1 potential for the peptide.
b. Fraction of total trajectories which shatter.
c. Number of different fragmentation pathways.

Table 5. Mechanisms of Soft-Landing for ala_2-H^+ + F-SAM Collisions[a]

E_i (eV)	Phys-Pen-Phys	Pen-Phys-Pen	Pen-Phys	Phys-Pen	Phys
5	4 ± 1	21 ± 2	19 ± 2	15 ± 2	25 ± 2
13.5	2 ± 1	17 ± 2	30 ± 3	3 ± 1	13 ± 2

a. $\theta_i = 0^o$. Percentages of trapped trajectories that followed a particular mechanism are listed.

Figure Captions

Figure 1. (A) Top and side view of H–terminated diamond{111} surface models with 8 C layers and one unit cell. The unit cell depicts the tetrahedral arrangement of each C atom. Color code: C atoms – black, and H atoms – light gray.

(B) Schematic diagram of the chemically modified F–SAM surface. The two embedded QM regions in the surface, a single chain (red box) and the single chain with a QM buffer region (blue box), are also depicted. Only the propyl tip of a chain is present in the QM region with the last CF_2 group acting as a linking atom shown in green above. The chemically modified chain consists of the propyl tip substituted with either the –COCl or –CHO head group. Adapted with permission from reference 21.

Figure 2. Intermolecular potential energy curves for CF_4/CH_4 calculated at the MP2/aug–cc–pVTZ level (solid circles) and fitted analytic potential (solid lines). The curves emphasize the following interactions: A, C – C; B, C – H; C, F – H; and D, F – C. Color code for the atoms: C – black, H – light gray, F – purple. Adapted with permission from reference 32.

Figure 3. Comparison between IPECs calculated at the MP2/aug–cc–pVTZ level (solid circles) for CF_4 interacting with the $–NH_2$ group of $HCONH_2$ and those predicted with the analytic potentials (solid lines) using parameters listed in Table 2 of ref 32. Color code: C – black, H – light gray, F – purple, N – blue. Adapted with permission from reference 32.

Figure 4. Comparison of experimental and simulation $P(\Delta E_{int})$ for E_i =13.5 and 22.5 eV for θ_i = 0^o. For the curve identified as "0.86 x Expt data" the experimental distribution is scaled by 18/21, where 18 and 21 are the average percentages of E_i transferred to ΔE_{int} in the simulations and experiments, respectively. Adapted with permission from reference 14.

Figure 5. Effect of peptide ion intramolecular potential on energy transfer. Distributions of energy transfer to E_{int}, E_{surf}, and E_f for $gly_2–H^+$ collisions with the diamond {111} surface at E_i = 70 eV (1614 kcal/mol) and $\theta_i = 45^o$. Simulations with the AMBER (– – –) and AM1 (—) models for the $gly_2–H^+$ intramolecular potential are compared. Adapted with permission from reference 15.

Figure 6. Structures and potential energies for ala_2-H^+ binding with a CF_3-$(CF_2)_7$-S- F-SAM surface. Adapted with permission from reference 32.

Figure 7. Distribution of the average fraction of the ala_2-H^+ eleven heavy atoms which penetrate the F-SAM, f_{pen}, for the trajectories which are trapped on/in the F-SAM at the conclusion of the trajectories.[44] Simulations for E_i of 5 and 13.5 eV, with $\theta_i = 0^o$. Adapted with permission from reference 44.

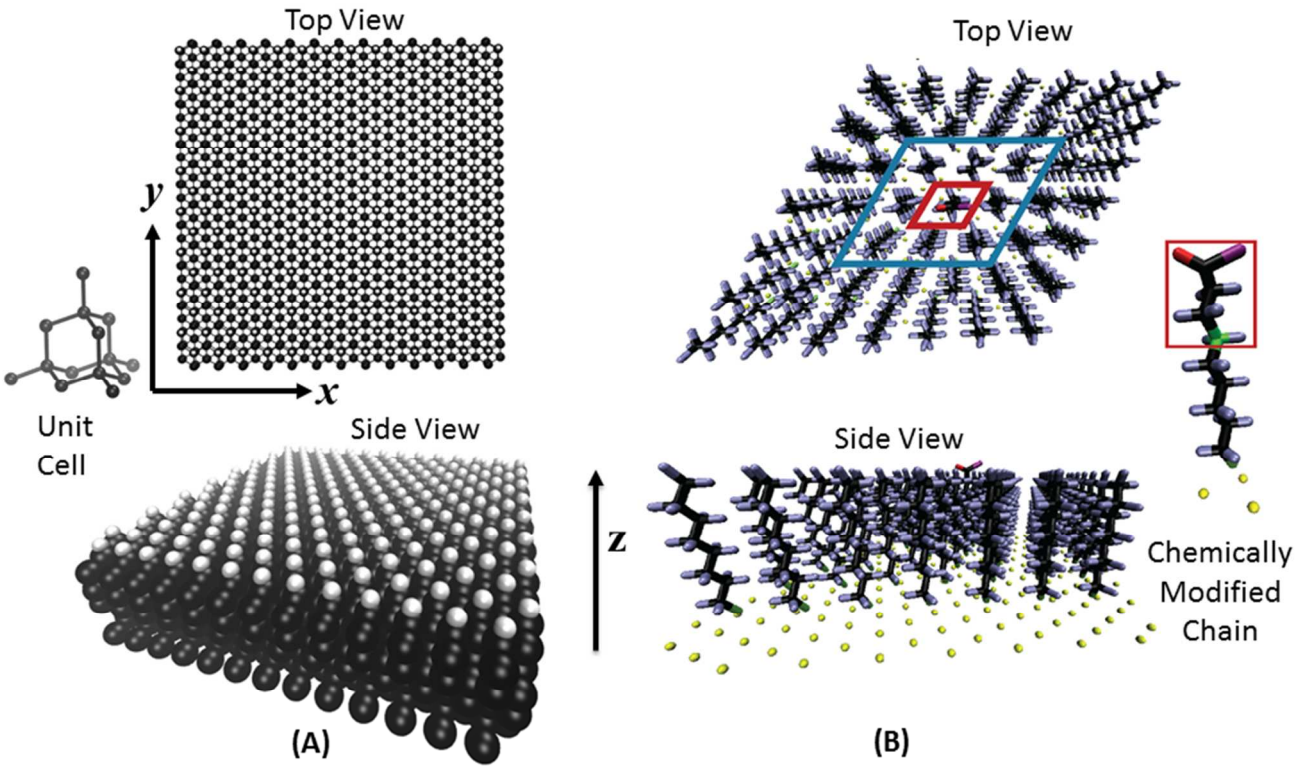
Top View
y
x
Unit
Cell
Side View
(A)
z
Top View
Side View
Chemically
Modified
Chain
(B)

Figure 1.

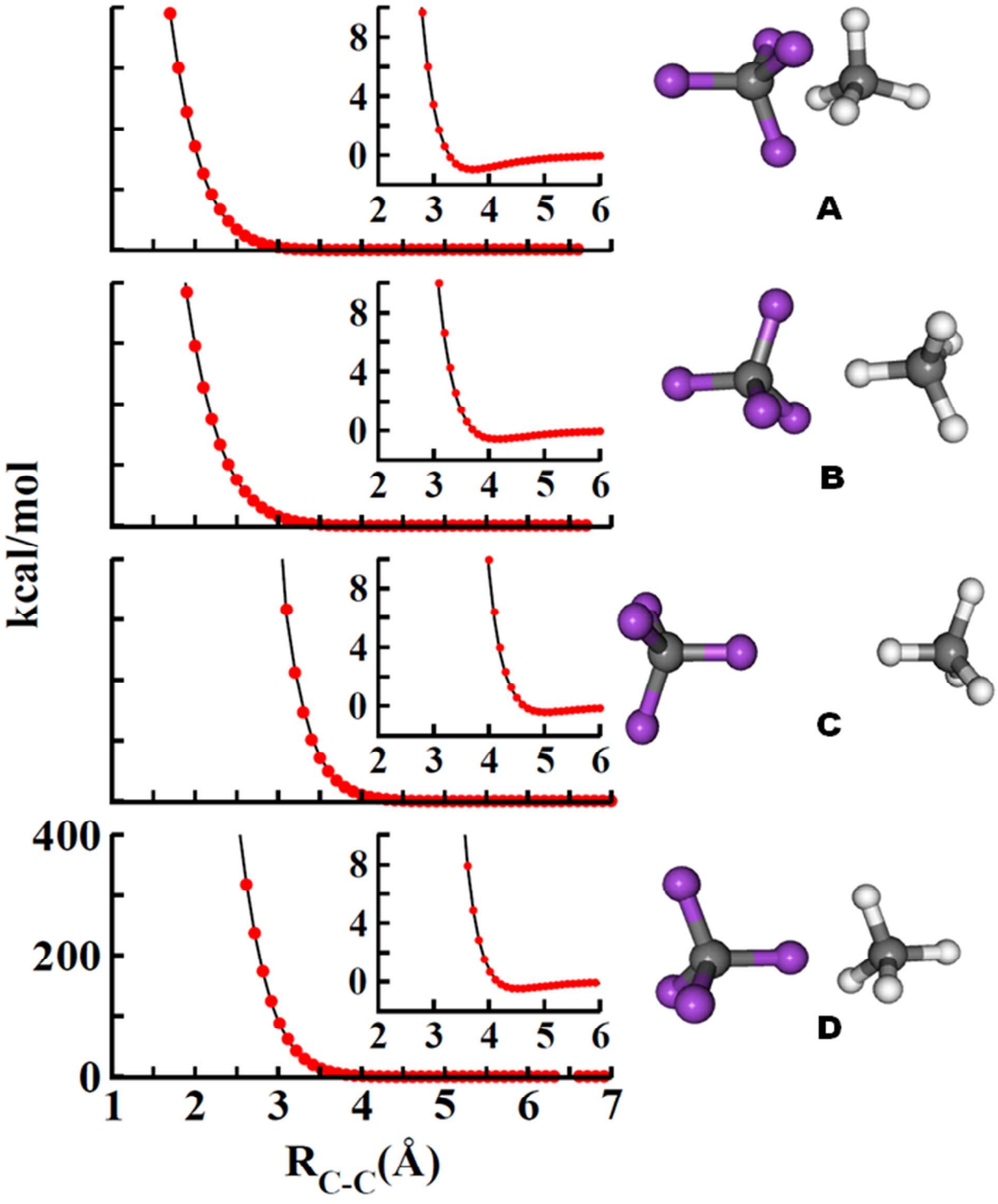

Figure 2.

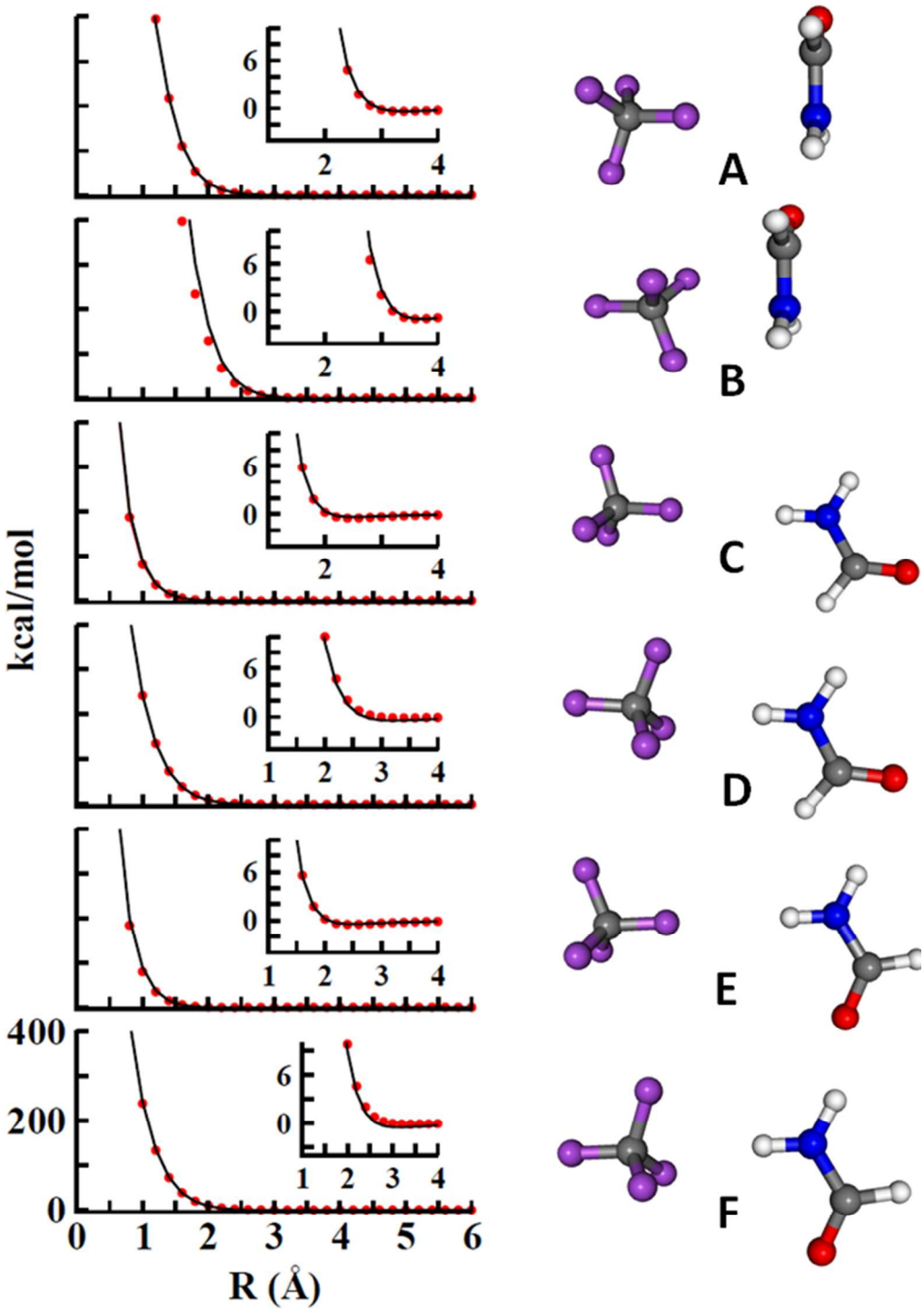

Figure 3.

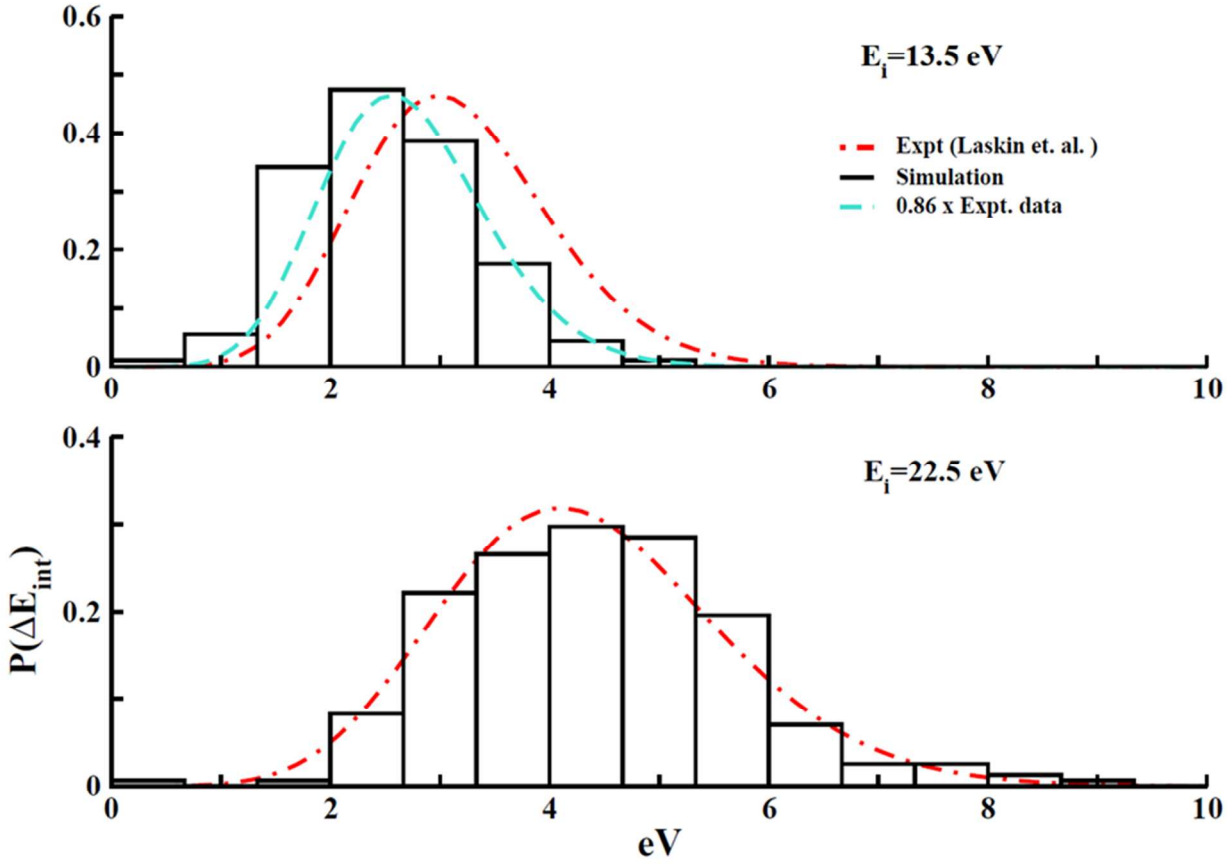
E_i=13.5 eV
Expt (Laskin et. al.)
Simulation
0.86 x Expt. data
E_i=22.5 eV
P(ΔE_int)
eV
0
0.2
0.4
0.6
0
2
4
6
8
10

Figure 4.

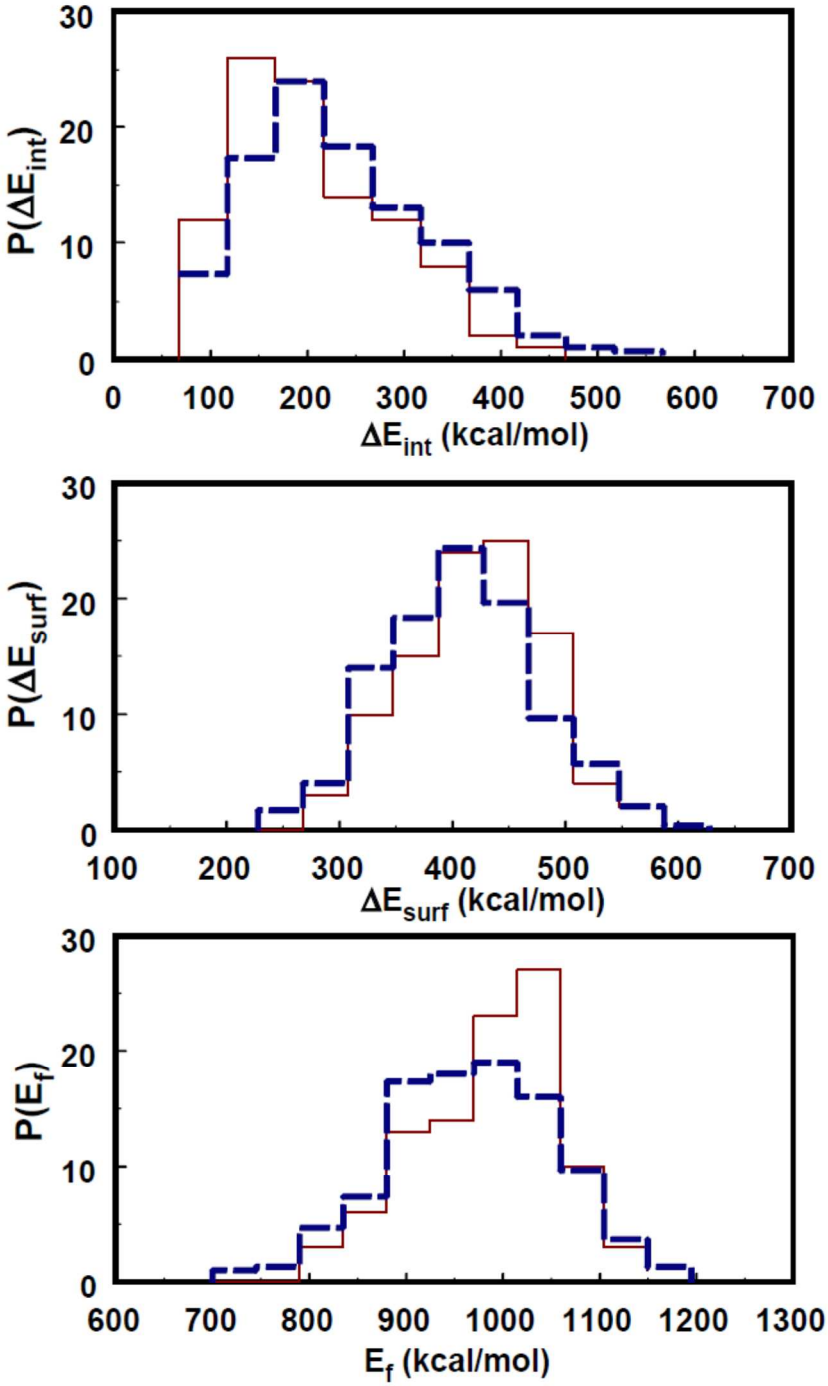
30
20
10
0
P(ΔE_int)
0 100 200 300 400 500 600 700
ΔE_int (kcal/mol)
30
20
10
0
P(ΔE_surf)
100 200 300 400 500 600 700
ΔE_surf (kcal/mol)
30
20
10
0
P(E_f)
600 700 800 900 1000 1100 1200 1300
E_f (kcal/mol)

Figure 5.

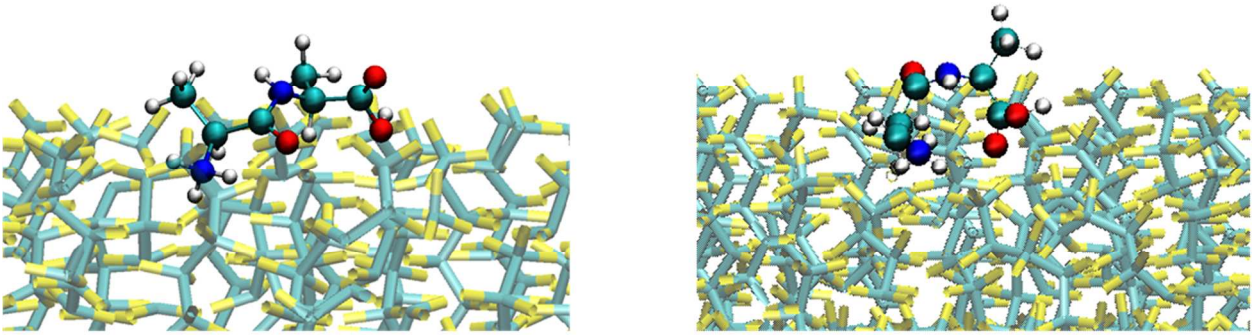

$E_b \approx -10$ kcal/mol $E_b \approx -14$ kcal/mol

Figure 6.

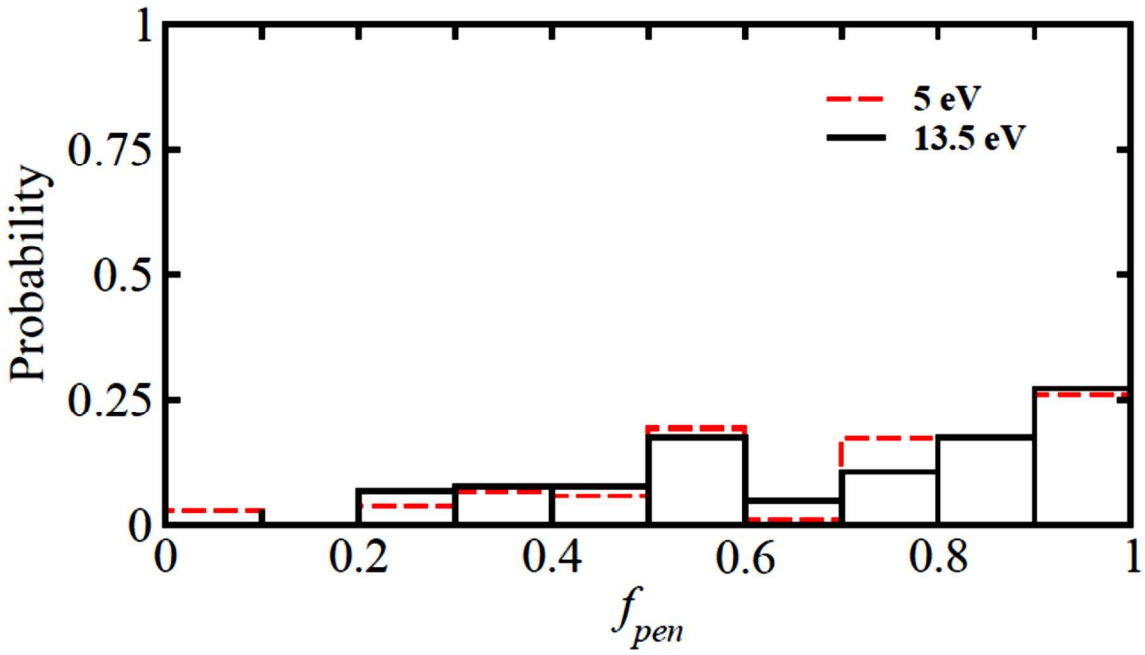

Figure 7.